Nano Research 2015, 8(12): 3982–3991
DOI 10.1007/s12274-015-0901-0
Research Article
ISSN 1998-0124
CN 11-5974/O4

Stable metallic 1T-WS_2 ultrathin nanosheets as a promising agent for near-infrared photothermal ablation cancer therapy

Qin Liu[1,§], Chunyang Sun[2,§], Qun He[1], Adnan Khalil[1], Ting Xiang[1], Daobin Liu[1], Yu Zhou[1], Jun Wang[2] (✉), and Li Song[1] (✉)

[1] *National Synchrotron Radiation Laboratory, University of Science and Technology of China, Hefei 230029, China*
[2] *Hefei National Laboratory for Physical Science at the Microscale, School of Life Sciences, University of Science and Technology of China, Hefei 230027, China*
[§] *These authors contributed equally to this work.*

Received: 8 July 2015
Revised: 7 September 2015
Accepted: 19 September 2015

KEYWORDS
hydrothermal, ammonium ion-intercalated 1T-WS_2, ultrathin nanosheets, biocompatibility, photostability, photothermal therapy

ABSTRACT

In this study, we present the preparation of stable 1T-WS_2 ultrathin nanosheets with NH_4^+ intercalation using a bottom-up hydrothermal method and the potential application of this material in light-induced photothermal cancer therapy. Our results revealed that nanosheets with a size of 150 nm were highly hydrophilic and exhibited strong light absorption and excellent photostability in the broad near-infrared wavelength region. The *in vitro* experimental results indicated good biocompatibility of the nanosheets. More notably, our *in vivo* antitumor experiments illustrated that light-induced photothermal ablation originating from irradiation of the 1T-WS_2 nanosheets with an 808 nm laser could efficiently kill tumor cells; these effects were obtained not only at the cellular level but also in the living organs of mice. This result may lead to new applications of two-dimensional layered materials in novel photothermal therapies and other photothermal related fields.

1 Introduction

Near-infrared (NIR) laser-induced photothermal ablation (PTA) therapy is considered, in recent years, a gentle, less invasive, efficient, and potentially highly effective treatment that can be used as an alternative or supplement to conventional cancer treatments (surgery, radiation therapy, and chemotherapy). The NIR window usually refers to a specific range of wavelengths (700–1,300 nm) in which light has great penetration depth in biological tissues [1]. In principle, PTA therapy takes advantage of NIR absorbing

Address correspondence to Li Song, song2012@ustc.edu.cn; Jun Wang, jwang699@ustc.edu.cn

materials to transduce light at these wavelengths into heat, which can kill cancer cells and destroy tumors in mice [2]. Consequently, the absorption of tissue-penetrating NIR light is a prerequisite for PTA agents. In addition, good biocompatibility, high photostability, and high photothermal conversion efficiency are also indispensable for NIR laser-induced PTA agents. Therefore, to meet the strict requirements of PTA therapy, developing novel kinds of photothermal agents is highly desirable. Four types of photothermal agents have been studied extensively. The first type is noble metal nanostructures, such as Pd-based nanosheets and various Au nanostructures [3–12], which exhibit intense NIR photoabsorption and good performance for PTA therapy. The second type is carbon-based materials, including carbon nanotubes and graphene, which are generally hydrophobic and thus require complex surface modifications in order to be useful in aqueous environments [13–15]. The third type is organic compounds, e.g., indocyanine green (ICG) and polyaniline nanoparticles [16–18]. The last type is metal chalcogenide semiconductors and metal oxide nanostructures, including copper chalcogenide semiconductors, PEGylated $W_{18}O_{49}$ nanowires, and chemically exfoliated sulfide nanosheets [19–27]. Among these potential PTA agents, two-dimensional (2D) layered transition metal dichalcogenides (TMDs) have attracted tremendous attention recently, but challenges are still faced in relation to these materials. The synthesis of 1T-TMD nanosheets is restricted to the conventional "lithium intercalated exfoliation" route, in which n-butyllithium endows the 2D nanosheets with an ultrathin structure and a metallic phase. However, the as-synthesized, toxic alkali-metal-intercalated TMDs are highly reactive products that are sensitive to moisture, temperature, and even aging [28, 29]. Moreover, extra surface functionalization of the nanostructures with specific chemical groups (e.g., PEG) is necessary to realize good biocompatibility for use in PTA therapy. Therefore, it is crucial to explore rational n-butyllithium-free synthetic routes to achieve stable 1T-TMDs with good biocompatibility and photostability, which could provide a versatile synthetic alternative and optimize the PTA performance of these materials. In this work, we report the successful synthesis of unique ammonium ion-intercalated 1T-WS_2 ultrathin nanosheets (abbreviated as N-WS_2 NSs) with very good biocompatibility and photostability via a facile hydrothermal method. The as-prepared nanosheets are not only highly hydrophilic, but also exhibit strong absorption in the broad NIR region (800–1,200 nm). Notably, the nanostructures exhibit high stability for several months and good biocompatibility. The measured high photothermal conversion efficiency and the results of *in vitro* and *in vivo* antitumor experiments further demonstrate that the nanosheets are very promising NIR agents for practical use in PTA therapy. This research may also stimulate new syntheses and applications of TMD materials in photothermal therapy, as well as in other biomedical research areas and applications.

2 Experimental

2.1 Synthesis of N-WS_2 nanosheets

A hydrothermal reaction was used to synthesize ammonia-intercalated WS_2 ultrathin nanosheets in a sealed autoclave system. Ammonium tungstate hydrate ($(NH_4)_{10}W_{12}O_{41}{\cdot}xH_2O$, AR) and thiourea ($CS(NH_2)_2$, AR) were purchased from Shanghai Chemical Reagent Co., Ltd. All reagents were analytical grade and used as received without further purification. For the synthesis, 0.5 mmol $(NH_4)_{10}W_{12}O_{41}{\cdot}xH_2O$ and 30 mmol thiourea were dissolved in 35 mL distilled water under vigorous stirring to form a homogeneous solution. Then, the solution was transferred into a 45 mL Teflon-lined stainless steel autoclave, maintained at 220 ℃ for 36 h, and naturally cooled to room temperature. The final black product was washed with absolute ethanol several times and dried at 60 ℃ under vacuum.

2.2 *In vitro* photothermal therapy

HeLa cells, MDA-MB-231 cells, and HepG2 cells were obtained from the American Type Culture Collection (ATCC) and cultured in Dulbecco's modified Eagle medium (DMEM, Gibco) supplemented with 10% fetal bovine serum (FBS, Hyclone, Thermo Scientific). To determine the cytotoxicity of N-WS_2 NSs, cells were seeded into 96-well plates with different concentrations of nanosheets for 24 h. The relative cell viabilities were determined by the methyl thiazolyltetrazolium (MTT)

assay according to previously reported methods [30]. To assess the effect of photothermal therapy, HeLa cells were seeded in 96-well plates and incubated with N-WS_2 NSs for 6 h, followed by irradiation with an 808 nm laser for 10 min.

2.3 *In vivo* photothermal cancer therapy

Female NOD/SCID mice were obtained from Beijing HFK Bioscience Co., Ltd. and used at 6 weeks of age. Experiments were performed following ethical guidelines, and all animals received care in compliance with the guidelines outlined in the Guide for the Care and Use of Laboratory Animals. The procedures were approved in advance by the Animal Care and Use Committee at the University of Science and Technology of China. The xenograft tumor model was generated by subcutaneous injection of 4×10^6 HeLa cells suspended in 100 μL phosphate buffered saline (PBS, with 30% Matrigel, BD Bioscience) into the right shoulder of each mouse. When the tumor volume grew to approximately 60 mm^3, the mice were randomly divided into 4 equivalent groups.

2.4 Photothermal therapy

One group of mice bearing HeLa tumors were intratumorally injected with 40 μL of 1.2 $mg \cdot mL^{-1}$ N-WS_2 NSs and were immediately irradiated with an 808 nm NIR laser (BWT Beijing Co., Ltd.) at a power density of 0.6 $W \cdot cm^{-2}$ for 10 min. The other mice groups were treated only with the same volume of PBS or N-WS_2 NSs, or laser irradiation power density. The temperature of the tumor sites was recorded by an IR 7320 thermal camera and analyzed with the IR Flash Software (Infrared Cameras. Inc.). The tumor sizes and weights were monitored every day. The tumor volume was calculated with the formula $V = 0.5 \times \text{length} \times \text{width}^2$. For the blood and H&E analyses, samples of the tumors and blood were sent to the First Affiliated Hospital of Anhui Medical University.

2.5 Characterization

The samples were characterized by X-ray powder diffraction (XRD) using a Philips X'Pert Pro Super diffractometer equipped with Cu Kα radiation (λ = 1.54178 Å). A JEM-2100F field emission electron microscope with an acceleration voltage of 200 kV was used to collect high-resolution transmission electron microscopy (TEM) images. The high-angle annular dark-field scanning transmission electron microscopy (HAADF-STEM) images were obtained with a Titan Cs-corrected Chemi-STEM (80 kV) atomic resolution analytical microscope. The size analyses were carried out in aqueous solution using a Malvern Zetasizer Nano ZS90 dynamic light scattering (DLS) instrument with a He-Ne laser (633 nm) and 90° collecting optics. UV-Vis-NIR absorption spectra were recorded with a Perkin Elmer Lambda 950 UV-Vis-NIR spectrophotometer. X-ray photoelectron spectroscopy (XPS) measurements were performed on a VG ESCALAB MK II X-ray photoelectron spectrometer equipped with a Mg Kα (1,253.6 eV) source. The binding energies obtained in the XPS spectral range were corrected for specimen charging effects using the C 1s level at the energy of 284.5 eV as a reference.

3 Results and discussion

The N-WS_2 NSs were synthesized via a modified method, according to our previous reports [31]. Figure 1(a) shows a typical TEM image of the as-prepared sample. Notably, the synthetic samples with uniform sheet-like morphology exhibit obvious ripples and corrugations, indicating a flexible and ultrathin nature. Atomic force microscope (AFM) image and line-scan profiles showed that the thickness of the N-WS_2 NSs was around 6.8 nm (Fig. S1 in the Electronic Supplementary Material (ESM)). In comparison to findings for previously reported 1T-WS_2 nanoribbons, the XRD and XPS characterizations carried out on the nanosheets (Figs. S2 and S3 in the ESM) showed similar peaks. This suggests that the nanosheets also consist of the 1T-WS_2 phase, which is highly stabilized by ammonium ion intercalation (N-WS_2). The HAADF-STEM image in Fig. 1(b) shows a unique zigzag chain superlattice with a W–W bond length of 2.7 Å, which further confirms the 1T phase of the nanosheets [32]. The DLS data in Fig. 1(c) revealed that the size of the N-WS_2 NSs is ca. 150 nm with no large agglomerates. It is worth noting that the N-WS_2 NSs are highly hydrophilic and can be readily dispersed in water, where they show the Tyndall effect owing to the

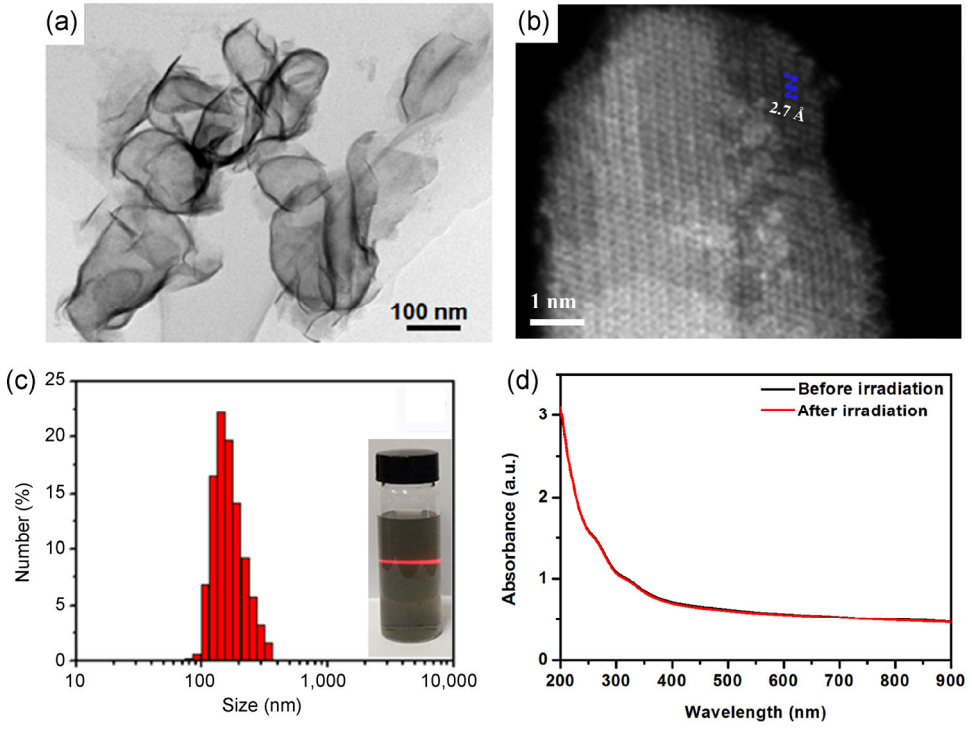

Figure 1 (a) Typical TEM image of as-prepared N-WS_2 nanosheets. (b) A typical HAADF-STEM image of N-WS_2 nanosheets reveals W–W bonds in an obvious zigzag chain superlattice. (c) The size distribution of the nanosheets measured by DLS. (d) UV-Vis-NIR spectra of aqueous N-WS_2 nanosheet dispersions before and after laser irradiation at a power density of 0.6 W·cm^{-2} for 1 h.

modified ammonia ions (inset, Fig. 1(c)). We found that aqueous dispersions of N-WS_2 NSs were extremely stable and no aggregation occurred even after 1 year. The UV-Vis-NIR absorption spectra of N-WS_2 NSs shown in Fig. 1(d) displays enhanced optical absorption as the wavelength increases from 200 to 900 nm. This indicates the strong light-absorption ability of N-WS_2 NSs, which motivated us to study the photothermal effects of this material. In addition, Fig. 1(d) shows the UV-Vis-NIR spectra of aqueous N-WS_2 NSs dispersions before and after laser irradiation at a power density of 0.6 W·cm^{-2} for 1 h.

Owing to such strong optical absorption in the NIR region, the synthetic N-WS_2 NSs are predicted to be promising agents for NIR laser-induced PTA therapy. We carried out a systematic study of our samples for cancer therapy by using deep tissue penetration and precise spatial control of an NIR laser. The temperature curve provided in Fig. 2(a) shows the temperature of aqueous dispersions containing N-WS_2 NSs at different concentrations (0–1.2 mg·mL^{-1}) under irradiation with an 808 nm wavelength laser at a power of 0.6 W·cm^{-2} (a value considered safe for human skin exposure) [33]. The temperature of the aqueous dispersions with N-WS_2 NSs (0.6 or 1.2 mg·mL^{-1}) dramatically increased from 19 to 53 ℃ within 5 min, whereas the temperature of pure water (without N-WS_2 NSs) increased by less than 1 ℃. We note here that the heating rate was slower after a further increase of the temperature owing to faster heat loss at higher temperatures. The temperature behavior clearly showed that the strong optical absorption in the NIR range allowed N-WS_2 NSs to quickly and efficiently convert NIR laser energy into heat. Moreover, compared with the poor stability of exfoliated 1T-WS_2 (Fig. S4 in the ESM) and the poor photostability of the widely used gold nanorods, which are also expensive, the UV-Vis-NIR spectra (Fig. 1(d)) of aqueous N-WS_2 NSs dispersions exhibited excellent photostability without any significant decrease in optical absorbance, even after laser irradiation for 1 h at a power density of 0.6 W·cm^{-2}. The stability of N-WS_2 NSs can be ascribed to the *in situ* bottom-up synthesis method and the structures intercalated with ammonia ions [31].

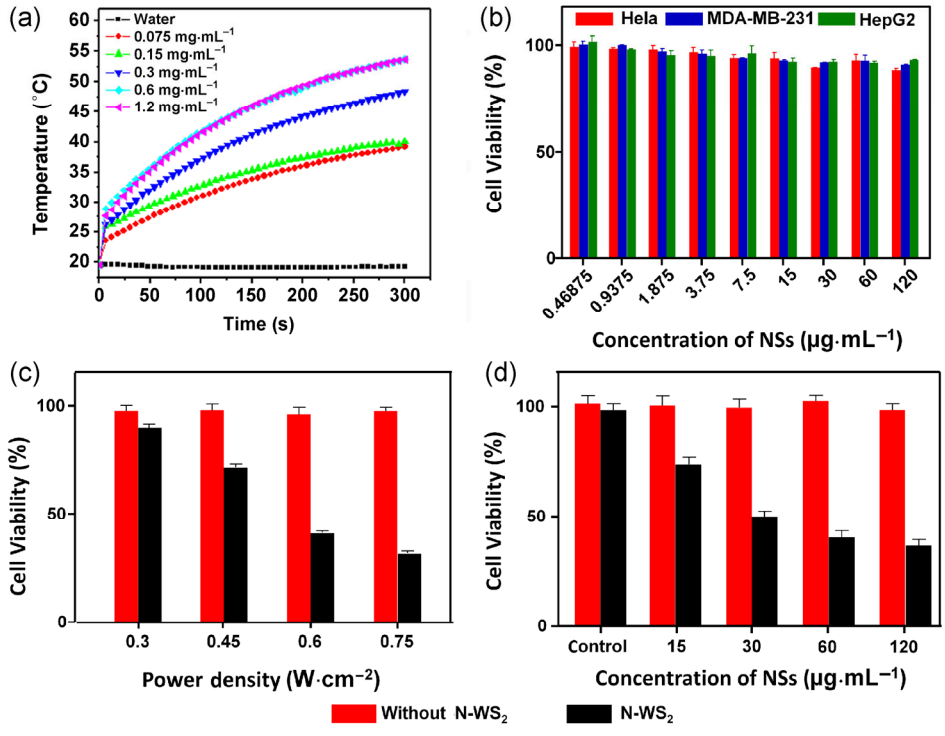

Figure 2 (a) The temperature increases for various concentrations of N-WS_2 nanosheet dispersions vs. NIR laser irradiation time at a power density of 0.6 W·cm^{-2}. (b) The viability of HeLa cells, MDA-MB-231 cells, and HepG2 cells after incubation with various concentrations of N-WS_2 nanosheets for 24 h. (c) The viability of HeLa cells cultured with N-WS_2 nanosheets at 120 μg·mL^{-1} with or without laser irradiation for 10 min. Error bars are based on the standard deviations of three parallel samples. (d) The viability of HeLa cells cultured with various concentrations of N-WS_2 nanosheets and then irradiated at a power density of 0.6 W·cm^{-2} for 10 min.

For biological applications, ideal photothermal coupling agents have to be biocompatible. To evaluate the cytotoxicity of N-WS_2 NSs, HeLa cells (human cervical carcinoma cell line), MDA-MB-231 cells (human mammary epithelial cell line), and HepG2 cells (human hepatocellular carcinoma cell line) were cultured. The cytotoxicity was studied by a standard MTT assay after 24 h. The estimated cellular viability (Fig. 2(b)) was >90% after 24 h, even at the highest N-WS_2 NSs concentration of 120 μg·mL^{-1}. No significant differences in cell proliferation were observed among the three cell lines, indicating the good biocompatibility of N-WS_2 NSs with cells. We claim that an aqueous dispersion containing N-WS_2 NSs with a concentration of less than 120 μg·mL^{-1} can be considered to have negligible cytotoxicity. Compared with the previous use of Li-exfoliated 1T-WS_2, which had a cell viability of 40% at a concentration of 100 μg·mL^{-1} owing to the usage of n-butyllithium (extremely toxic and difficult to remove completely), for photothermal therapy, our synthesized N-WS_2 NSs modified with around 4 at.% ammonium ions exhibited good biocompatibility.

First, the PTA capacity of N-WS_2 NSs was examined *in vitro* by using the HeLa cell line and the MTT assay. We incubated HeLa cancer cells with N-WS_2 NSs at a concentration of 120 μg·mL^{-1} for 6 h and then irradiated them with an 808 nm NIR laser at different power densities (0.3, 0.45, 0.6, and 0.75 W·cm^{-2}). The cell viability (Fig. 2(c)) was >95% without laser irradiation and decreased as a function of the power density. The proliferation rate of HeLa cells was only ~25% of the control after laser irradiation at a power density of 0.75 W·cm^{-2}. Meanwhile, we measured the cell viability at a fixed laser power density of 0.6 W·cm^{-2} with different concentrations of N-WS_2 NSs. The cell viability (Fig. 2(d)) decreased to ~80% at a concentration of 15 μg·mL^{-1} and further decreased to ~40% at a concentration of 120 μg·mL^{-1}. It is worth noting that the control groups were not affected by laser irradiation at 0.6 W·cm^{-2}, indicating that cancer cells are essentially unharmed by irradiation at this power density, and

that the ablation could be attributed to the observed photothermal effect of N-WS_2 NSs.

To further analyze the therapeutic capabilities, we investigated the photothermal effect of N-WS_2 NSs during *in vivo* NIR irradiation experiments using NOD/SCID mice bearing HeLa tumors. In our experiments, 40 μL of N-WS_2 NSs and PBS were injected intratumorally into the female mice, followed by irradiation using an 808 nm NIR laser at a power density of 0.6 W·cm^{-2}. Thermal images (Figs. 3(a)–3(d)) of the regions of interest were recorded at different time intervals using an infrared camera. We analyzed the average surface temperature of the tumor sites throughout the photothermal therapy using the IR Flash Software. The average temperature of the tumors in the PBS group without NIR irradiation remained constant at ~28 ˚C, and similar behavior was observed for the non-irradiated N-WS_2 NSs group. In one of the control experiments, a slight increase (~3 ˚C) in temperature was detected due to laser heating when the tumors alone were exposed to NIR. Interestingly, the temperature of the tumors in the N-WS_2 NSs group that was exposed to NIR laser irradiation increased dramatically to 50 ˚C (an increase of ~21 ˚C) within 4 min and subsequently remained around 50 ˚C for the next 6 min. We note here that the temperature increased only in a small area around the tumor site, whereas other organs were not affected owing to the spatial control of the laser irradiation (Fig. 3(e)). We consider the concentration of nanosheets and power density used in the experiments adequate for effective tumor treatment. Indeed, as demonstrated in the available literature, tumors can be completely destroyed in ~5 min with a temperature increase greater than 15 ˚C [30, 34, 35].

Finally, we performed tumor treatment with N-WS_2 NSs *in vivo* using NOD/SCID mice bearing HeLa tumors. Mice bearing HeLa tumors were randomly divided into four groups (five mice each) when the average tumor size reached 60 mm^3. One dose of the N-WS_2 NSs was injected intratumorally in the N-WS_2 and N-WS_2+NIR groups (concentration and power density were the same as in the imaging experiment), while other groups received only PBS or NIR irradiation. The tumor sizes (Fig. 4(a)) were monitored using a capillary every 2 days and calculated with the following formula: 0.5 × length × $width^2$. In the control groups, i.e., mice that received only NIR irradiation, injection of PBS, or injection of N-WS_2 NSs, the tumor growth was not inhibited. We observed that after 14 days, the dimensions of the tumors in the control groups were about 12 times greater than the initial tumor size. On the contrary, all of the tumors in the N-WS_2+NIR group disappeared after 4 days of irradiation owing to the large temperature change induced by the N-WS_2 NSs photothermal process. It is also worth noting that no tumor recurrence was observed after the whole treatment process. Furthermore, we monitored the body weight of the mice to evaluate the influence of the various treatments.

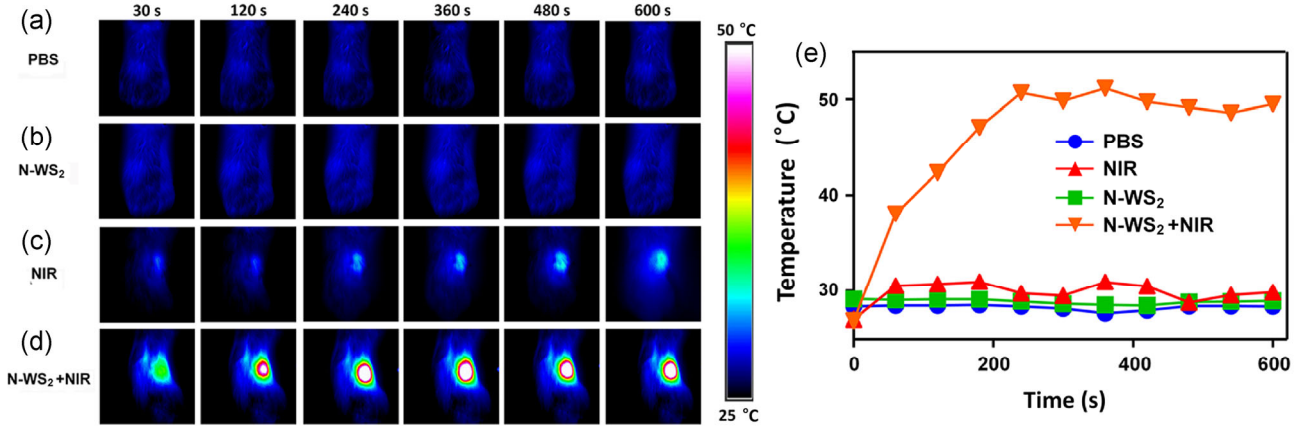

Figure 3 Thermal infrared images at different time intervals of tumor-bearing mice treated with N-WS_2 nanosheets and NIR laser irradiation at 0.6 W·cm^{-2} (d). As control experiments, other mice groups received only PBS injection (a), N-WS_2 nanosheet injection (b), or laser irradiation (c). (e) Temperature in the tumor sites for different groups of mice vs. the irradiation time.

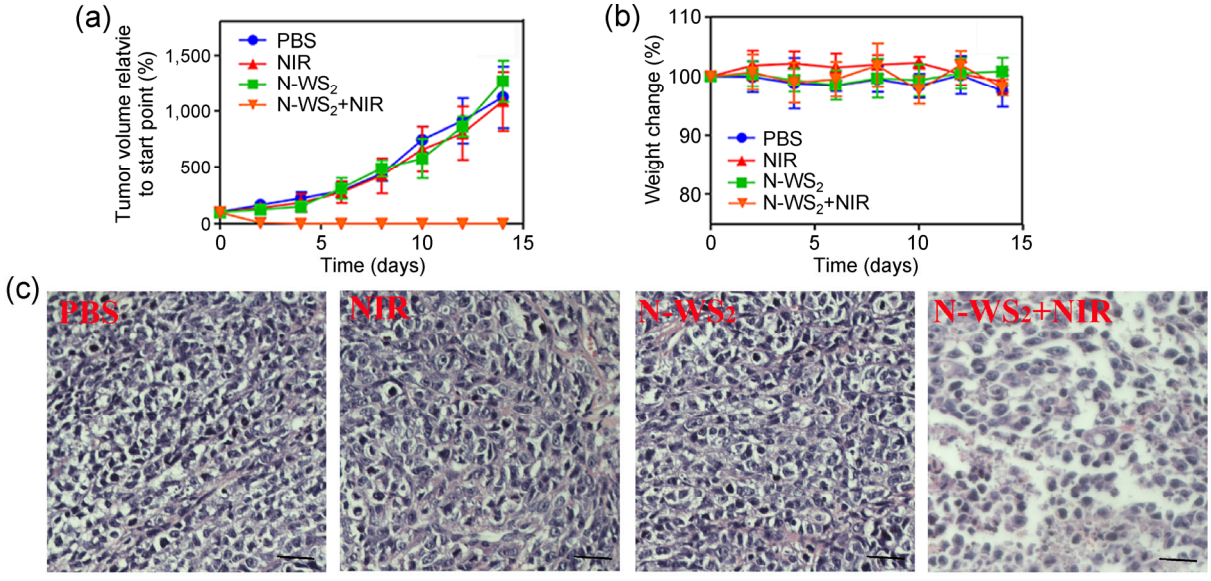

Figure 4 (a) The growth of the tumors after different treatments on HeLa-bearing NOD/SCID mice (n = 5). (b) The body weight of the mice during the different photothermal therapies. (c) H&E analysis of tumors collected 2 days after the initial treatment. Scale bar = 50 μm.

The weight of the mice (Fig. 4(b)) was relatively stable and remained within normal values in all groups, suggesting very promising biocompatibility and low toxicity of the *in vivo* N-WS_2 NSs PTA treatment. The autopsy showed no abnormalities in the liver, lung, and other organs, further demonstrating the low systemic toxicity of intratumoral injection of N-WS_2 NSs and NIR irradiation. In order to clarify the mechanism of photothermal therapy, we collected tumors for H&E staining (Fig. 4(c)) after 2 days of irradiation treatment. Compared with the control groups (PBS, NIR, or N-WS_2 NSs treatment only), significant cell damage was observed in the N-WS_2 NSs group undergoing NIR laser irradiation. Collectively, these results suggested that the elimination of tumors in the N-WS_2+NIR group was a result of the photothermal therapy itself, and was not due to the toxicity of the N-WS_2 NSs.

In addition, blood analysis was carried out on the 6th and 16th days of the treatment process to evaluate possible negative effects of the NIR photothermal therapy. A complete blood panel, including white blood cells (WBC), red blood cells, hemoglobin, hematocrit, platelets, mean corpuscular volume, mean corpuscular hemoglobin concentration, and mean corpuscular hemoglobin, was carried out. It can be seen from Fig. 5 that all of the parameters had relative normal values in the N-WS_2+NIR group, except the WBC count. The WBC count slightly decreased after the 6th day of treatment, which could be attributed to inflammation after the photothermal therapy, similar to our previous observations [36]. Notably, the WBC count recovered to the same value as that of the control group by the 16th day, further indicating the low negative effect of N-WS_2 NSs agents for mice during PTA of tumors. Based on the above observations, we claim that the higher temperature induced by N-WS_2 NSs is optimal for photothermal therapy, killing tumor cells not only at the cellular level but also in the living organs of an animal.

4 Conclusions

In summary, we have successfully synthesized unique 1T-WS_2 ultrathin nanosheets using a facile and environmentally friendly hydrothermal method. The as-prepared 1T-WS_2 ultrathin nanosheets exhibited good photostability and high photothermal conversion efficiency owing to their strong optical absorption in the NIR range. The observations from *in vitro* and *in vivo* experiments revealed that the N-WS_2 NSs rapidly and efficiently converted the energy from an 808 nm laser into heat. Subsequently, the higher temperature induced by N-WS_2 NSs could kill tumor cells, not only at the cellular level but also in the living organs

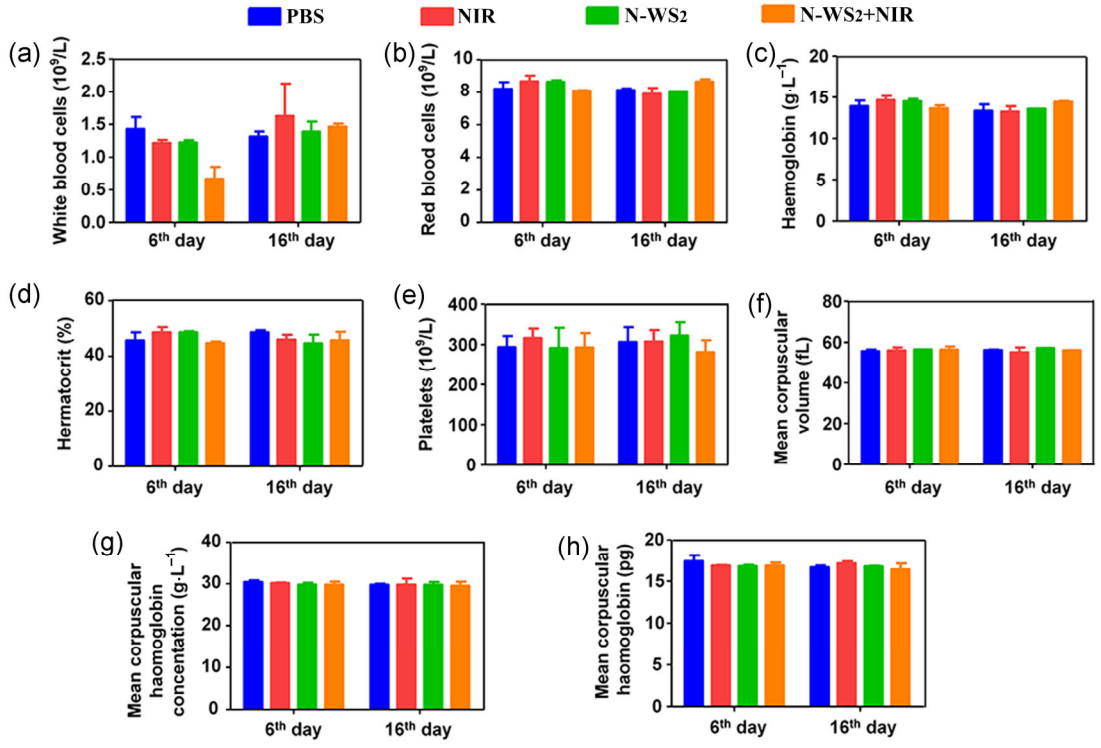

Figure 5 Blood analysis during *in vivo* experiments for (a) white blood cells, (b) red blood cells, (c) hemoglobin, (d) hematocrit, (e) platelets, (f) mean corpuscular volume, (g) mean corpuscular hemoglobin concentration, and (h) mean corpuscular hemoglobin of the PBS (blue column), NIR (red column), N-WS_2 (green column), and N-WS_2+NIR (orange column) group.

of mice. These results provide a clear description of the light-induced thermal behavior of layered 1T-WS_2 intercalations, and thus may trigger intensive future studies of 2D layered materials for cancer therapeutics.

Electronic Supplementary Material: Supplementary material (XRD pattern and XPS analysis of N-WS_2) is available in the online version of this article at http://dx.doi.org/10.1007/s12274-015-0901-0.

Acknowledgements

We acknowledge the financial support of the National Basic Research Program of China (Nos. 2012CB825800, 2014CB848900, and 2014CB932500), the Science Fund for Creative Research Groups of the National Natural Science Foundation of China (No. 11321503), the National Natural Science Foundation of China (Nos. U1232131, U1532112, 11321503, 51222202, 91123010, and 11574280) and the Fundamental Research Funds for the Central Universities (No. WK2310000035). L. S. thanks the recruitment program of global experts, the CAS Hundred Talent Program. The authors would like to acknowledge Prof. Chuanhong Jin from the Center of Electron Microscopy of Zhejiang University for the assistance on HAADF-STEM.

References

[1] Jöbsis-vanderVliet, F. F. Discovery of the near-infrared window into the body and the early development of near-infrared spectroscopy. *J. Biomed. Opt.* **1999**, *4*, 392–396.

[2] Huang, X. H.; El-Sayed, I. H.; Qian, W.; El-Sayed, M. A. Cancer cell imaging and photothermal therapy in the near-infrared region by using gold nanorods. *J. Am. Chem. Soc.* **2006**, *128*, 2115–2120.

[3] Tang, S. H.; Chen, M.; Zheng, N. F. Sub-10-nm Pd nanosheets with renal clearance for efficient near-infrared photothermal cancer therapy. *Small* **2014**, *10*, 3139–3144.

[4] Wang, S. T.; Chen, K. J.; Wu, T. H.; Wang, H.; Lin, W. Y.; Ohashi, M.; Chiou, P. Y.; Tseng, H. R. Photothermal effects of supramolecularly assembled gold nanoparticles for the targeted treatment of cancer cells. *Angew. Chem., Int. Ed.* **2010**, *49*, 3777–3781.

[5] Wang, J.; Zhu, G. Z.; You, M. X.; Song, E. Q.; Shukoor, M. I.; Zhang, K. J.; Altman, M. B.; Chen, Y.; Zhu, Z.; Huang, C. Z.; Tan, W. H. Assembly of aptamer switch probes and photosensitizer on gold nanorods for targeted photothermal and photodynamic cancer therapy. *ACS Nano* **2012**, *6*, 5070–5077.

[6] Ke, H. T.; Wang, J. R.; Dai, Z. F.; Jin, Y. S.; Qu, E. Z.; Xing, Z. W.; Guo, C. X.; Yue, X. L.; Liu, J. B. Gold-nanoshelled microcapsules: A theranostic agent for ultrasound contrast imaging and photothermal therapy. *Angew. Chem., Int. Ed.* **2011**, *50*, 3017–3021.

[7] You, J.; Zhang, G. D.; Li, C. Exceptionally high payload of doxorubicin in hollow gold nanospheres for near-infrared light-triggered drug release. *ACS Nano* **2010**, *4*, 1033–1041.

[8] Yavuz, M. S.; Cheng, Y. Y.; Chen, J. Y.; Cobley, C. M.; Zhang, Q.; Rycenga, M.; Xie, J. W.; Kim, C.; Song, K. H.; Schwartz, A. G. et al. Gold nanocages covered by smart polymers for controlled release with near-infrared light. *Nat. Mater.* **2009**, *8*, 935–939.

[9] Ye, E. Y.; Win, K. Y.; Tan, H. R.; Lin, M.; Teng, C. P.; Mlayah, A.; Han, M. Y. Plasmonic gold nanocrosses with multidirectional excitation and strong photothermal effect. *J. Am. Chem. Soc.* **2011**, *133*, 8506–8509.

[10] Yuan, H.; Fales, A. M.; Vo-Dinh, T. TAT peptide-functionalized gold nanostars: Enhanced intracellular delivery and efficient NIR photothermal therapy using ultralow irradiance. *J. Am. Chem. Soc.* **2012**, *134*, 11358–11361.

[11] Terentyuk, G.; Panfilova, E.; Khanadeev, V.; Chumakov, D.; Genina, E.; Bashkatov, A.; Tuchin, V.; Bucharskaya, A.; Maslyakova, G.; Khlebtsov, N. et al. Gold nanorods with a hematoporphyrin-loaded silica shell for dual-modality photodynamic and photothermal treatment of tumors *in vivo*. *Nano Res.* **2014**, *7*, 325–337.

[12] Liu, Y.; Yin, J.-J.; Nie, Z. H. Harnessing the collective properties of nanoparticle ensembles for cancer theranostics. *Nano Res.* **2014**, *7*, 1719–1730.

[13] Kim, J. W.; Galanzha, E. I.; Shashkov, E. V.; Moon, H. M.; Zharov, V. P. Golden carbon nanotubes as multimodal photoacoustic and photothermal high-contrast molecular agents. *Nat. Nanotechnol.* **2009**, *4*, 688–694.

[14] Wang, X. J.; Wang, C.; Cheng, L.; Lee, S.-T.; Liu, Z. Noble metal coated single-walled carbon nanotubes for applications in surface enhanced Raman scattering imaging and photothermal therapy. *J. Am. Chem. Soc.* **2012**, *134*, 7414–7422.

[15] Hu, S.-H.; Chen, Y.-W.; Hung, W.-T.; Chen, I. W.; Chen, S.-Y. Quantum-dot-tagged reduced graphene oxide nanocomposites for bright fluorescence bioimaging and photothermal therapy monitored *in situ*. *Adv. Mater.* **2012**, *24*, 1748–1754.

[16] Yu, J.; Javier, D.; Yaseen, M. A.; Nitin, N.; Richards-Kortum, R.; Anvari, B.; Wong, M. S. Self-assembly synthesis, tumor cell targeting, and photothermal capabilities of antibody-coated indocyanine green nanocapsules. *J. Am. Chem. Soc.* **2010**, *132*, 1929–1938.

[17] Yang, J.; Choi, J.; Bang, D.; Kim, E.; Lim, E. K.; Park, H.; Suh, J. S.; Lee, K.; Yoo, K. H.; Kim, E. K. et al. Convertible organic nanoparticles for near-infrared photothermal ablation of cancer cells. *Angew. Chem.* **2011**, *123*, 461–464.

[18] Song, X. J.; Chen, Q.; Liu, Z. Recent advances in the development of organic photothermal nano-agents. *Nano Res.* **2015**, *8*, 340–354.

[19] Zhou, M.; Zhang, R.; Huang, M.; Lu, W.; Song, S. L.; Melancon, M. P.; Tian, M.; Liang, D.; Li, C. A chelator-free multifunctional [^{64}Cu]CuS nanoparticle platform for simultaneous micro-PET/CT imaging and photothermal ablation therapy. *J. Am. Chem. Soc.* **2010**, *132*, 15351–5358.

[20] Hessel, C. M.; Pattani, V. P.; Rasch, M.; Panthani, M. G.; Koo, B.; Tunnell, J. W.; Korgel, B. A. Copper selenide nanocrystals for photothermal therapy. *Nano Lett.* **2011**, *11*, 2560–2566.

[21] Lakshmanan, S. B.; Zou, X. J.; Hossu, M.; Ma, L.; Yang, C.; Chen, W. Local field enhanced Au/CuS nanocomposites as efficient photothermal transducer agents for cancer treatment. *J. Biomed. Nanotechnol.* **2012**, *8*, 883–890.

[22] Tian, Q. W.; Tang, M. H.; Sun, Y. G.; Zou, R. J.; Chen, Z. G.; Zhu, M. F.; Yang, S. P.; Wang, J. L.; Wang, J. H.; Hu, J. Q. Hydrophilic flower-like CuS superstructures as an efficient 980 nm laser-driven photothermal agent for ablation of cancer cells. *Adv. Mater.* **2011**, *23*, 3542–3547.

[23] Tian, Q. W.; Jiang, F. R.; Zou, R. J.; Liu, Q.; Chen, Z. G.; Zhu, M. F.; Yang, S. P.; Wang, J. L.; Wang, J. H.; Hu, J. Q. Hydrophilic Cu_9S_5 nanocrystals: A photothermal agent with a 25.7% heat conversion efficiency for photothermal ablation of cancer cells *in vivo*. *ACS Nano* **2011**, *5*, 9761–9771.

[24] Chen, Z. G.; Wang, Q.; Wang, H. L.; Zhang, L. S.; Song, G. S.; Song, L. L.; Hu, J. Q.; Wang, H. Z.; Liu, J. S.; Zhu, M. F. et al. Ultrathin PEGylated $W_{18}O_{49}$ nanowires as a new 980 nm-laser-driven photothermal agent for efficient ablation of cancer cells *in vivo*. *Adv. Mater.* **2013**, *25*, 2095–2100.

[25] Chou, S. S.; Kaehr, B.; Kim, J.; Foley, B. M.; De, M.; Hopkins, P. E.; Huang, J. X.; Brinker, C. J.; Dravid, V. P. Chemically exfoliated MoS_2 as near-infrared photothermal agents. *Angew. Chem., Int. Ed.* **2013**, *52*, 4160–4164.

[26] Cheng, L.; Liu, J. J.; Gu, X.; Gong, H.; Shi, X. Z.; Liu, T.; Wang, C.; Wang, X. Y.; Liu, G.; Xing, H. Y. et al. PEGylated WS_2 nanosheets as a multifunctional theranostic agent for *in vivo* dual-modal CT/photoacoustic imaging guided photothermal therapy. *Adv. Mater.* **2014**, *26*, 1886–1893.

[27] Liu, Q.; Sun, C. Y.; He, Q.; Liu, D. B.; Khalil, A.; Xiang, T. Wu, Z. Y.; Wang, J.; Song, L. Ultrathin carbon layer coated MoO_2 nanoparticles for high-performance near-infrared photothermal cancer therapy. *Chem. Commun.* **2015**, *51*, 10054–10057.

[28] Ohuchi, F. S.; Jaegermann, W.; Pettenkofer, C.; Parkinson, B. A. Semiconductor to metal transition of WS_2 induced by K intercalation in ultrahigh vacuum. *Langmuir* **1989**, *5*, 439–442.

[29] Zak, A.; Feldman, Y.; Lyakhovitskaya, V.; Leitus, G.; Popovitz-Biro, R.; Wachtel, E.; Cohen, H.; Reich, S.; Tenne, R. Alkali metal intercalated fullerene-like MS_2 (M = W, Mo) nanoparticles and their properties. *J. Am. Chem. Soc.* **2002**, *124*, 4747–4758.

[30] Yang, J.; Wang, H. Y.; Yi, W. J.; Gong, Y. H.; Zhou, X.; Zhuo, R. X.; Zhang, X. Z. PEGylated peptide based reductive polycations as efficient nonviral gene vectors. *Adv. Healthcare Mater.* **2013**, *2*, 481–489.

[31] Liu, Q.; Li, X. L.; Xiao, Z. R.; Zhou, Y.; Chen, H. P.; Xiang, T.; Xu, J. Q.; Chu, W. S.; Wu, X. J.; Yang, J. L. et al. Stable metallic 1T-WS_2 nanoribbons intercalated with ammonia ions: The correlation between structure and electrical/optical properties. *Adv. Mater.* **2015**, *27*, 4837–4844.

[32] Voiry, D.; Yamaguchi, H.; Li, J. W.; Silva, R.; Alves, D. C. B.; Fujita, T.; Chen, M. W.; Asefa, T.; Shenoy, V. B.; Eda, G. et al. Enhanced catalytic activity in strained chemically exfoliated WS_2 nanosheets for hydrogen evolution. *Nat. Mater.* **2013**, *12*, 850–855.

[33] Timko, B. P.; Dvir, T.; Kohane, D. S. Remotely triggerable drug delivery systems. *Adv. Mater.* **2010**, *22*, 4925–4943.

[34] Peng, C. L.; Shih, Y. H.; Lee, P. C. Hsieh, T. M. H.; Luo, T. Y.; Shieh, M. J. Multimodal image-guided photothermal therapy mediated by ^{188}Re-labeled micelles containing a cyanine-type photosensitizer. *ACS Nano* **2011**, *5*, 5594–5607.

[35] Zhang, J. L.; Jin, W.; Wang, X. Q.; Wang, J. C.; Zhang, X.; Zhang, Q. A novel octreotide modified lipid vesicle improved the anticancer efficacy of doxorubicin in somatostatin receptor 2 positive tumor models. *Mol. Pharmaceutics* **2010**, *7*, 1159–1168.

[36] Yang, K.; Xu, H.; Cheng, L.; Sun, C. Y.; Wang, J.; Liu, Z. *In vitro* and *in vivo* near-infrared photothermal therapy of cancer using polypyrrole organic nanoparticles. *Adv. Mater.* **2012**, *24*, 5586–5592.